PNAS RESEARCH ARTICLE | BIOCHEMISTRY

Extracellular nanobody screening using conformationally stable GPCR variants

Xin Zhang[a,b,1], Kaixuan Gao[a,b,1], Jia Nie[c,1], Hengyu Meng[a], Xiaoou Sun[b,d], Jiawei Zhao[b,d,2], and Xiangyu Liu[a,b,3]

Edited by Aashish Manglik, University of California, San Francisco, CA; received April 19, 2025; accepted September 23, 2025 by Editorial Board Member Yifan Cheng

G protein–coupled receptors (GPCRs) are prominent drug targets that have attracted intensive efforts in drug screening. Binding-based screening methods for GPCR ligands often require conformationally stable, purified receptors. However, obtaining large quantities of GPCRs in stable states, particularly with unoccupied extracellular ligand-binding pockets and especially in their active conformations, remains challenging due to the inherent dynamic nature of these receptors. To address this challenge, we propose a universal approach for stabilizing GPCRs in specific conformations. Using the M1 muscarinic acetylcholine receptor (M1R) as a model, we successfully stabilized M1R in its active conformation through de novo design of a fusion protein, and further demonstrated the generalizability of this strategy by applying it to other GPCRs. We screened a synthetic yeast display library of nanobodies against both the stabilized active-state and previously reported inactive-state M1R, identifying several nanobodies that specifically recognize each conformation. This method not only facilitates the stabilization of GPCRs in desired states but also provides valuable tools for developing more selective therapeutic agents, enhancing drug discovery efficiency and specificity.

GPCR | cryo-EM structure | protein design | nanobody

Significance

We present a universal strategy to stabilize G protein–coupled receptors (GPCRs) in defined conformational states, overcoming challenges posed by their intrinsic dynamics. Through de novo design of fusion proteins to lock the M1 muscarinic receptor in its active conformation and screening synthetic nanobody libraries against distinct states, we identified conformation-specific binders. This platform enables precise targeting of GPCR functional states and accelerates discovery of selective therapeutics, offering transformative potential for GPCR drug development.

G protein–coupled receptors (GPCRs) are central mediators of signal transduction across cell membranes, regulating nearly every aspect of human physiology. Their pivotal role in modulating physiological processes has made GPCRs prime therapeutic targets. Notably, approximately 34% of all FDA-approved drugs function by modulating GPCR activities (1). Despite extensive pharmacological and structural studies that have elucidated the mechanisms by which ligands stimulate or inhibit these receptors, drug discovery efforts targeting GPCRs still face significant challenges. A particularly pressing challenge is the development of conformation-selective and subtype-selective ligands (2, 3).

The conformational flexibilities of GPCRs complicates the direct enrichment of conformation specific ligands. GPCRs typically exist in a spectrum of conformations between two primary states: the inactive state and the active state (4). The prominent conformational change occurs in the intracellular region, particularly in Transmembrane Helix 6 (TM6), while the dynamics in the extracellular region, which contains the orthosteric pocket, are relatively minor (5, 6). These subtle conformational changes do not prevent the binding of antagonists or agonists but instead modulate their affinity for receptors in different states (7). Identifying ligands that recognize these subtle conformational changes is crucial for discovering function-specific ligands.

Binding-based experimental screening techniques that utilize purified receptors, such as DNA-encoded libraries (DEL), yeast surface displayed libraries, and phage displayed libraries, present a promising approach encompassing chemical space exploration and conformational selection (8–11). A pivotal challenge in this context is obtaining conformation-stable purified receptors, particularly in their active states, which are thermodynamically unstable. Molecular dynamics studies on receptors such as the beta-2 adrenergic receptor (β2AR), μ-opioid receptor (μOR), and muscarinic acetylcholine receptor 2 (M2R) have demonstrated the instability of active conformations (12–16). Single-molecule studies reveal that under apo conditions or when bound with antagonists or partial agonists, these receptors predominantly remain in the inactive state. Even in the presence of full agonists, the receptor fluctuates between active and inactive states (17, 18). This transient active state poses a significant obstacle for agonist screening. To address this issue, full agonists, G proteins, or G protein mimics have been employed to stabilize the active state during screening (19–21). Although these strategies achieve some success, they also come with limitations. Full agonists occupy the orthosteric pocket, making it impossible to screen for other orthosteric agonists. Moreover, the resulting receptor-G protein or receptor-G protein mimic complexes are often unstable, with dissociation disrupting the screening process (22). Therefore, there is an urgent

Author affiliations: [a]State Key Laboratory of Membrane Biology, Tsinghua-Peking Center for Life Sciences, School of Pharmaceutical Sciences, Tsinghua University, Beijing 100084, China; [b]Research Center for Biological Structure, Beijing Advanced Innovation Center for Structural Biology, Tsinghua University, Beijing 100084, China; [c]Department of Obstetrics, Xiangya Hospital Central South University, Changsha 410013, China; and [d]School of Medicine, Tsinghua University, Beijing 100084, China

Author contributions: X.Z., K.G., J.Z., and X.L. designed research; X.Z., K.G., J.N., H.M., and X.L. performed research; X.S. contributed new reagents/analytic tools; X.Z., K.G., and J.N. analyzed data; and X.Z., K.G., and X.L. wrote the paper.

The authors declare no competing interest.

This article is a PNAS Direct Submission. A.M. is a guest editor invited by the Editorial Board.

[1]X.Z., K.G., and J.N. contributed equally to this work.

[2]Present address: Department of Biological Chemistry and Molecular Pharmacology, Harvard Medical School, Boston, MA 02115.

[3]To whom correspondence may be addressed. Email: liu_xy@mail.tsinghua.edu.cn.

This article contains supporting information online at https://www.pnas.org/lookup/suppl/doi:10.1073/pnas.2508879122/-/DCSupplemental.

Published November 4, 2025.

need for innovative strategies to design conformation-stable receptors that can effectively overcome these challenges.

Muscarinic acetylcholine receptors represent a prominent class of receptors that have attracted considerable attention as promising targets for addressing complicated neuropsychiatric disorders, including Alzheimer's disease, schizophrenia, and Parkinson's disease (23–26). Despite extensive efforts, only one drug based on the cholinergic mechanism, xanomeline combined with peripheral antagonist trospium chloride (KarXT), received FDA approval in 2024 for the treatment of schizophrenia (27, 28). A major hurdle has been the occurrence of cholinergic adverse effects, often resulting from the off-target activation of other muscarinic acetylcholine receptor subtypes, leading to the discontinuation of most clinical trials (25). Consequently, over the past decade, research in both academia and industry has focused on enhancing the subtype selectivity of muscarinic acetylcholine receptor modulators. Antibodies offer a promising solution to the challenges of developing subtype-selective ligands, given their ability to engage broader epitopes across receptor surface, thereby facilitating more selective binding (29–31). Notably, this targeting strategy maintains efficacy regardless of the antibody's pharmacological activity. Through conjugation with nonselective ligands, these antibodies form bifunctional constructs that synergistically integrate the antibody's exquisite targeting specificity with the ligand's functional modulation, thereby opening new avenues for developing GPCR modulators with subtype selectivity (32). However, the development of antibody-based modulators targeting the muscarinic acetylcholine receptor family remains largely unexplored.

Previously, we reported the de novo design of a fusion protein that locks M1R in an inactive state (33). In this study, we extended our design strategy to stabilize M1R in its active state. This approach resulted in a GPCR that remains in the active conformation even in the absence of agonist binding. Leveraging this design, we screened a series of nanobodies targeting M1R. Structural and pharmacological analyses revealed that these nanobodies function as active-state selective nanobodies or inactive-state selective nanobodies by interacting with the extracellular pocket of M1R. Together, our findings validate the conceptual feasibility of screening extracellular nanobodies targeting GPCRs using conformation-locked GPCRs and offer tools for drug discovery and mechanistic studies of M1R.

Results

Generation of Conformationally Stable M1R in Active State. With the advancements of generative protein design technology, it has become feasible to create a wide variety of proteins with shapes precisely tailored to specific requirements. A hallmark of GPCR activation is the outward movement of TM6. Our objective is to de novo design fusion proteins that connect TM5 and TM6, locking TM6 into either an inward or outward displacement, which stabilizes the receptor in its inactive or active conformation, respectively (Fig. 1*A*). Previously, we reported our approach for designing an inactive-state GPCR using a click fusion protein named Clip, which is rigidly linked to TM5 and TM6 to restrict the dynamic of TM6. For designing an active-state GPCR, the α5 helix of the G protein is employed to lock the outward movement state of TM6. Studies have demonstrated that the α5 helix of the G protein alone can stabilize the active state of the receptors such as β2-adrenergic receptor (β2AR) and opsin without the requirement for the intact G protein or engineered miniG protein (34–36). To implement this, the α5 helix was linked to the C terminus of the receptor via a 2× GGSGG linker, with a proline residue added at the N terminus of the α5 helix of G protein as a structural mark to terminate the linker and initiate α-helix formation (37). Meanwhile, a de novo designed fusion protein containing a binding pocket for the α5 helix of G protein was fused between TM5 and TM6 to stabilize the interaction between the receptor and the α5 helix of G protein (Fig. 1*B*). The cryo-EM structure of the active-state M1R bound to the G_{11} protein (PDB: 6OIJ) served as the reference structure model. Initially, the receptor chain and the α5 helix of the G_{11} protein (residues 335 to 359, ENIRFVFAAVKDTILQLNLKEYNLV, G_{11}CT) were retained from the original model. Subsequently, the backbone of the fusion protein was generated between TM5 and TM6 using RFdiffusion, forming a suitable binding pocket to stabilize the position of the G_{11}CT. Sequence design was performed using ProteinMPNN and structure prediction was conducted using AlphaFold2-Multimer. Two sequences with high pLDDT scores were selected and synthesized, named M1R-G_{11}CT and M1R-G_{11}CTb (Fig. 1*C* and *SI Appendix*, Fig. S1). While the two proteins share the same scaffold, their surface charge distributions exhibit significant differences (*SI Appendix*, Fig. S2 *A* and *B*).

Biochemical Characterization of M1R-G_{11}CT. Cell surface expression analysis reveals that both M1R-G_{11}CT and M1R-G_{11}CTb demonstrate improved expression levels compared to the wild-type M1R (*SI Appendix*, Fig. S2*C*). And the yield of purified M1R-G_{11}CT and M1R-G_{11}CTb proteins reaches approximately 500 μg per liter of cell culture. Notably, M1R-G_{11}CT and M1R-G_{11}CTb were purified in the absence of any ligand, similar to M1R-Clip1 (33). The purified proteins display excellent behavior during size-exclusion chromatography (SEC), as evidenced by the sharp and symmetrical peaks with minimal aggregation (Fig. 1*D* and *SI Appendix*, Fig. S2*D*). These characteristics suggest that M1R-G_{11}CT and M1R-G_{11}CTb proteins are intrinsically well-folded and homogeneous without the need for additional stabilizing ligands.

Previous studies have shown that M1R-ΔICL3, a widely utilized construct featuring a truncated intracellular loop 3 (ICL3), maintains functional properties similar to those of the wild-type M1R, including ligand binding profiles and receptor signaling capabilities (6). Radioligand binding assays were performed to validate the biochemical characterization of M1R-G_{11}CT and M1R-G_{11}CTb constructs. Saturation binding assays were conducted to determine the affinity of [^{3}H]-N-methylscopolamine (NMS) for these constructs. M1R-G_{11}CT and M1R-G_{11}CTb exhibit K_d values of 1.4 nM and 1.0 nM, respectively, comparable to the measured 1.1 nM for M1R-ΔICL3, indicating similar affinities for the antagonist NMS (*SI Appendix*, Fig. S2 *E–G*). Additionally, radioligand competition binding assays were conducted to evaluate the affinities of the agonist iperoxo and the antagonist atropine in these constructs. Compared to M1R-ΔICL3 (K_i = 1.9 nM), M1R-G_{11}CT and M1R-G_{11}CTb show similar binding affinities for atropine, with K_i values of 0.6 nM and 1.6 nM, respectively (*SI Appendix*, Fig. S2*H*). Remarkably, M1R-G_{11}CT and M1R-G_{11}CTb both display an approximately 600-fold higher binding affinity for the agonist iperoxo relative to M1R-ΔICL3 (Fig. 1*E*), representing one of the most significant enhancements among previously reported GPCR constructs (14, 21, 34, 38). These results suggest that M1R-G_{11}CT and M1R-G_{11}CTb have similar biochemical characterization and maintain a stable active state.

M1R-G_{11}CT Maintained Active-State Conformational Stability. We used M1R-miniGsq as a control to assess the conformational stability of M1R-G_{11}CT. M1R-miniGsq, a widely used construct

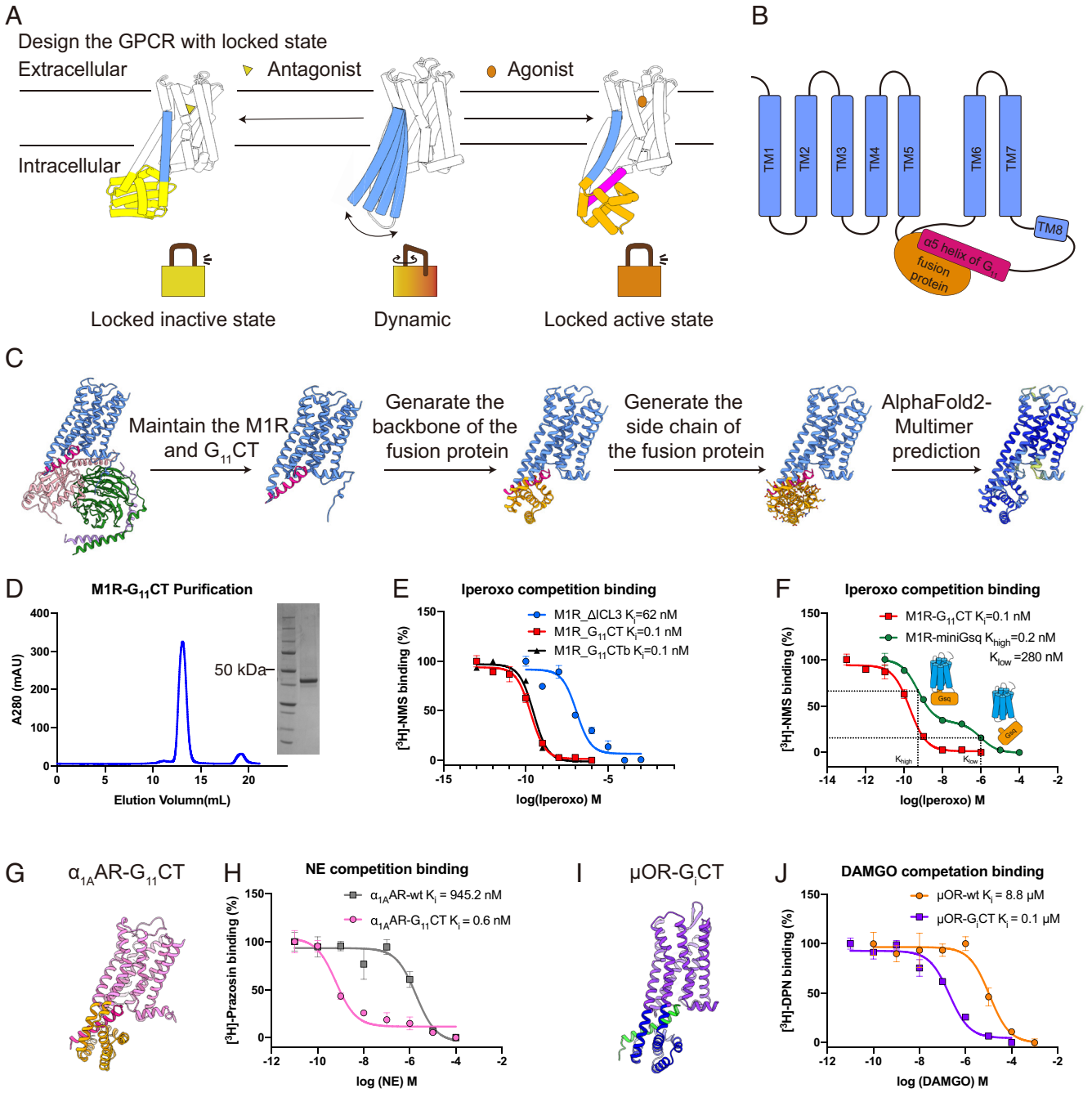

Fig. 1. Design and biochemical characterization of engineered active-state GPCR constructs. (*A*) Schematic representation of stabilizing GPCR in either the inactive or active state, with TM6 constrained in an inward or outward conformation using de novo designed fusion proteins. (*B*) Schematic representation of the M1R-G_{11}CT construct, featuring G_{11}CT fused to the C terminus of the receptor and the designed fusion protein inserted between TM5 and TM6 that accommodated the G_{11}CT. (*C*) Overview of the design process for the fusion protein of M1R-G_{11}CT. (*D*) SEC profile and corresponding SDS-PAGE analysis of M1R-G_{11}CT. (*E*) Competition binding assays with iperoxo reveal that both engineered constructs (M1R-G_{11}CT and M1R-G_{11}CTb) exhibit similarly enhanced agonist affinity. (*F*) Competition binding assays of M1R-G_{11}CT and M1R-miniGsq with iperoxo demonstrate the homogeneity and stability of M1R-G_{11}CT. (*G*) Structure of α_{1A}AR-G_{11}CT predicted by AlphaFold2-Multimer. (*H*) The α_{1A}AR-G_{11}CT construct exhibits a significantly higher binding affinity for norepinephrine (K_i = 0.6 nM) compared to α_{1A}AR-wt (K_i = 945.2 nM), representing a greater than 1,000-fold enhancement. (*I*) Structure of μOR-G_iCT predicted by AlphaFold2-Multimer. (*J*) The μOR-G_iCT construct exhibits significantly increased binding affinity for agonist DAMGO, with K_i values of 0.1 μM for μOR-G_iCT vs. 8.8 μM for wild-type μOR. Data are represented as mean ± SEM (n = 3).

for active-state structure determination, integrates miniGsq protein—which features a truncated alpha helical domain (AHD) and an α5 helix substitution from Gq protein—at the C terminus of the receptor. M1R-miniGsq exhibits a K_d value of 0.4 nM for [^{3}H]-NMS (*SI Appendix*, Fig. S2*I*). Of note, M1R-miniGsq exhibits a biphasic binding curve (K_{high} = 0.2 nM, K_{low} = 280 nM), indicating that only a fraction of receptor displays an increase in agonist affinity induced by G protein coupling. Similar biphasic curves were reported in other GPCR–G protein complexes (14, 39). In contrast, M1R-G_{11}CT exhibits a monophasic binding curve (K_i = 0.1 nM) (Fig. 1*F*), indicative of a homogeneous high-affinity agonist state akin to G protein–coupled M1R.

Design and Biochemical Characterization of α_{1A}AR-G_{11}CT and μOR-G_iCT. Following similar Clip transfer strategy as previously described (Fig. 1 *G* and *I* and *SI Appendix*, Fig. S3*A*) (33), we successfully extended the M1R-G_{11}CT fusion protein design to several other GPCRs, including G_q/G_{11}-coupled α1A-adrenergic receptor (α_{1A}AR) and G_i/G_o-coupled μ-opioid receptor (μOR), designated α_{1A}AR-G_{11}CT and μOR-G_iCT. AlphaFold2 predictions validate the structural viability of these designs, exhibiting high pLDDT scores (*SI Appendix*, Fig. S3 *B* and *C*). Furthermore, radioligand binding assays were performed to confirm the functional characterization of these constructs. Of note, the α_{1A}AR-G_{11}CT construct exhibits reduced affinity for antagonist [^{3}H]-prazosin (K_d = 23.1 nM) compared to wild-type receptor (K_d = 1.0 nM) (*SI Appendix*, Fig. S4 *A* and *B*). In contrast, no notable difference in binding affinity was observed for the antagonist tamsulosin between the α_{1A}AR-G_{11}CT construct (K_i = 1.0 nM) and the wild-type receptor (K_i = 0.7 nM) (*SI Appendix*, Fig. S4*C*). Interestingly, α_{1A}AR-G_{11}CT exhibits a dramatic (>1,000-fold) enhancement in binding affinity for the agonist norepinephrine (NE) relative to α_{1A}AR-wt (Fig. 1*H*). The μOR-G_iCT construct exhibits [^{3}H]-diprenorphine (DPN) binding affinity (K_d = 1.9 nM) comparable to that of wild-type μOR (K_d = 5.9 nM) (*SI Appendix*, Fig. S4 *D* and *E*). Competition binding assays demonstrate that μOR-G_iCT has enhanced affinity for the agonists BU72 and DAMGO, while maintaining wild-type level binding affinity for the antagonist naloxone (Fig. 1*J* and *SI Appendix*, Fig. S4 *F* and *G*). These results demonstrate the broad applicability of our method for stabilizing GPCRs in active conformations.

The Structure of M1R-G_{11}CT Represents Agonist-Free Active State. As described above, M1R-G_{11}CT demonstrate excellent biochemical properties throughout the purification process, even in the absence of agonist supplementation. We subsequently determined the cryo-EM structure of M1R-G_{11}CT without ligand at the resolution of 3.62 Å (Fig. 2*A* and *SI Appendix*, Fig. S5). Two-dimensional class averages clearly delineate the secondary structural features within both the transmembrane domain and the designed fusion protein, confirming the proper folding of the engineered receptor (Fig. 2*B*). The density map of the orthosteric pocket lacks the complete ligand density previously observed in the active-state M1R bound to iperoxo, supporting that the receptor is in a ligand-free state. However, a residual, undefined density remains at the position of its tertiary amine group, likely contributed by a cation in the buffer, such as sodium (*SI Appendix*, Fig. S6*A*). Moreover, the orthosteric pocket exhibits

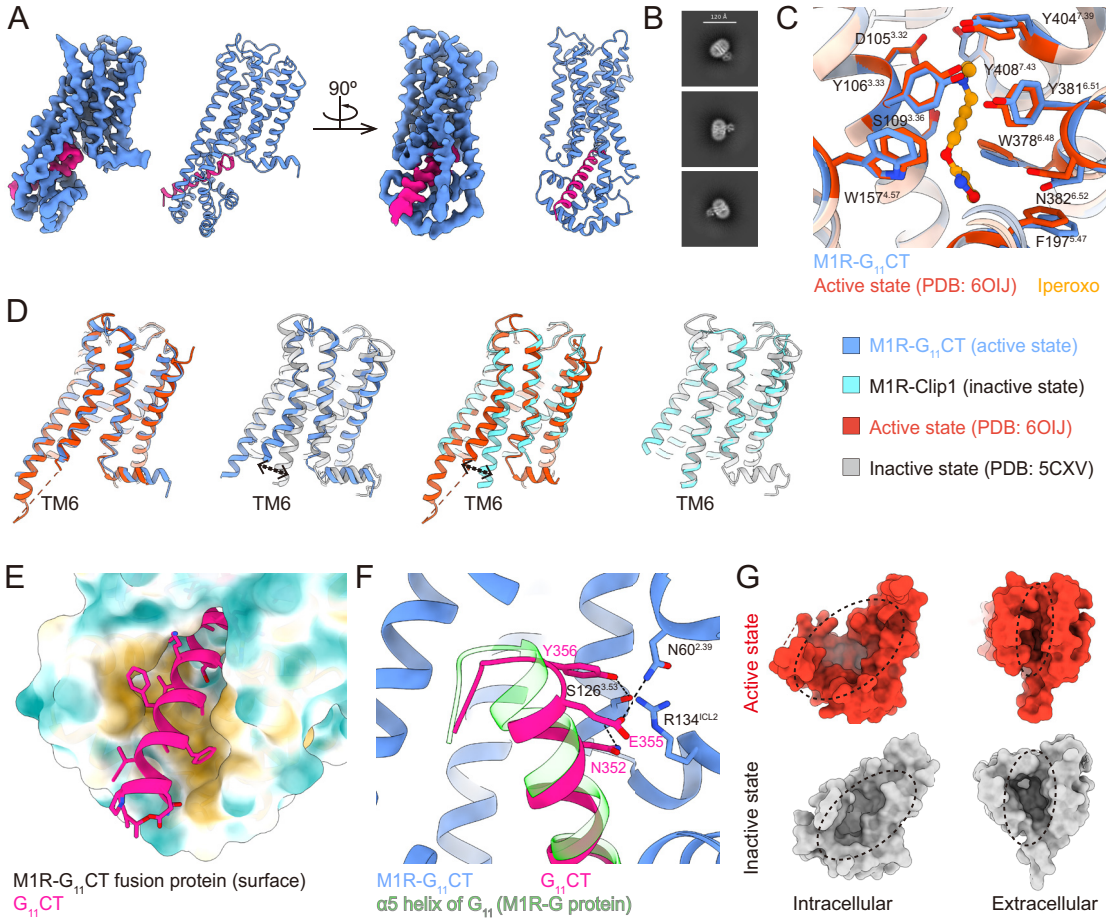

Fig. 2. The structure of M1R-G_{11}CT reveals its agonist-free active state. (*A*) Overall cryo-EM density map and atomic model of M1R-G_{11}CT. (*B*) Representative 2D class averages of M1R-G_{11}CT particles, highlighting the transmembrane helices of the receptor and the designed fusion protein. (*C*) The orthosteric binding pocket in M1R-G_{11}CT closely resembles that of the previously resolved active-state structure bound to iperoxo (PDB: 6OIJ), confirming its stabilization in an active receptor conformation. (*D*) Structural alignment of M1R-G_{11}CT and M1R-Clip1 with both active-state M1R (PDB: 6OIJ) and inactive-state M1R (PDB: 5CXV) structures, emphasizing the displacement of TM6. (*E*) The de novo designed fusion protein forms a hydrophobic binding pocket that accommodates the N terminus of G_{11}CT. (*F*) The C terminus of G_{11}CT adopts a binding pose analogous to the α5 helix of the G protein in the previously resolved M1R-G protein complex bound to iperoxo (PDB: 6OIJ), further validating its functional mimic of G protein interactions. (*G*) Top and bottom views comparing the extracellular and intracellular pockets of active-state and inactive-state M1R.

a conformation similar to that of the active-state M1R bound to the agonist iperoxo (Fig. 2*C*). And the experimentally determined structure exhibits remarkable congruence with our computational prediction, exhibiting a RMSD of 1.070 Å for all Cα atoms in the structured regions (residues 25 to 393 of receptor with designed fusion protein and G_{11}CT; flexible C terminus and N terminus excluded) (*SI Appendix*, Fig. S6*B*). This structural correspondence between experimental and predicted models underscores the reliability of our protein engineering approach.

Structure comparison was conducted between two engineered receptors (the inactive-state M1R-Clip1 and the active-state M1R-G_{11}CT) and their respective state-specific structures to evaluate the design outcomes (Fig. 2*D*). For M1R-Clip1, TM6 exhibits an inward displacement characteristic of the inactive state (PDB: 5CXV), differing from the outward movement observed in the active state (PDB: 6OIJ). Conversely, TM6 in M1R-G_{11}CT retains an outward displacement, maintaining the angle and position analogous to the active state, distinct from the inward displacement of the inactive state. The designed fusion protein of M1R-G_{11}CT forms a well-defined hydrophobic pocket that accommodates the G_{11}CT (Fig. 2*E*). The position and orientation of G_{11}CT within the intracellular pocket of M1R closely mirror those observed in the M1R-G_{11} protein complex (Fig. 2*F*). Of note, the G_{11}CT of ligand-free M1R-G_{11}CT can still precisely insert into the intracellular pocket of the receptor, indicating that the active state of M1R-G_{11}CT is preserved independently of agonist activation. Taken together, we have successfully engineered M1R proteins with conformational stability in both the inactive state (M1R-Clip1) and the active state (M1R-G_{11}CT) through biochemical and structural analyses, enabling binding-based drug screening. Importantly, M1R-G_{11}CT maintains active state even under agonist-free condition, representing an advancement compared to previous strategies for generating active-state receptor.

Intracellular Orthogonal Screening for Extracellular Nanobodies. In the realm of binding-based drug screening, extracellular antibody screening targeting Class A GPCRs has long been a challenge. The difficulty stems from the inherent asymmetry in the solvent-accessible surface area (SASA) between the intracellular and extracellular regions of class A GPCRs. The M1R receptor serves as an example, where the intracellular SASA (6372.9 $Å^2$, calculated using Chimera X) in its inactive state exceeds that of the extracellular region (4,548 $Å^2$). Furthermore, upon receptor activation, the intracellular SASA (8303.6 $Å^2$) expands while the extracellular SASA (4278.2 $Å^2$) becomes more contracted (Fig. 2*G*). This results in a preferential enrichment of antibodies targeting the intracellular region, whereas antibodies specific to the extracellular region—especially those recognizing the active state—are often disadvantaged and routinely excluded during conventional binding-based antibody screening.

To address these challenges, we define intracellularly orthogonal receptors as those sharing the identical extracellular structures but possessing distinct intracellular regions. Examples of such receptor pairs include the inactivated pair atropine-bound M1R-ΔICL3 and M1R-Clip1, as well as the activated pair iperoxo-bound M1R-G_{11}CT and M1R-G_{11}CTb. By employing these intracellularly orthogonal receptors in iterative rounds of cross-screening, it is feasible to directionally enrich antibodies targeting the extracellular pocket. In this study, we screened for extracellular nanobodies specific to the inactive and active states using the aforementioned receptor pairs as baits, respectively, from a synthetic nanobody library displayed on the yeast surface (Fig. 3 *A*–*C*). Several rounds of magnetic-activated cell sorting (MACS) and fluorescence-activated cell sorting (FACS) were performed with progressively reduced receptor concentration to enhance the affinity of the selected nanobodies (*SI Appendix*, Fig. S7). While fusion proteins enabled stabilization of M1R in ligand-free active or inactive states, the specific tyrosine lid creates spatial constraints that prevent the CDR3 loops of nanobodies from effectively accessing and traversing the orthosteric pocket. These structural considerations guided our focus toward identifying allosteric nanobodies targeting M1R.

Following screening, the single colonies of yeast were stained using fluorescently labeled atropine-bound M1R-Clip1 and iperoxo-bound M1R-G_{11}CT proteins to identify conformation-specific nanobodies (Fig. 3*D*), the inactive-state selective nanobodies (NbF3, NbF7, NbA12) and the active-state selective nanobody (Nb1B4) were selected for further validation. The binding affinities of these nanobodies were assessed via on-yeast titration assay (*SI Appendix*, Fig. S8 *A*–*D*). Following the purification of nanobodies, a Glo-sensor-based signaling assay was performed to assess their pharmacological properties. Among the nanobodies selective for the inactive state, NbF7, NbF3, and NbA12 were identified to reduce the Emax of acetylcholine (ACh), the endogenous agonist. Furthermore, in the β-arrestin recruitment assay, we demonstrated that NbA12 exhibits a certain degree of selectivity among the five subtypes (*SI Appendix*, Fig. S8*G*). Subtype selectivity across M1R-M3R was further characterized for all four nanobodies using on-yeast titration assay. Our results demonstrate that NbF3 exhibits comparable binding to M1R and M2R, but shows a clear preference for M1R over M3R. NbF7, NbA12, and Nb1B4 display markedly stronger binding to M1R compared to both M2R and M3R, which is consistent with the functional activity profile observed for NbA12 (*SI Appendix*, Fig. S8*F*). Additionally, these nanobody features are localized on the side opposite to Clip1 in the two-dimensional classification of cryo-EM data processing, indicating that these nanobodies bind extracellularly (Fig. 3 *E*–*G*). However, we could not detect the agonist activity of Nb1B4, likely because the protein tends to aggregate after purification (*SI Appendix*, Fig. S8*H*), which impedes the assessment of its function. To identify additional active-state selective nanobodies, we performed NGS to analyze the nanobodies' enrichment pattern of the active-state screening group (Fig. 3*H*). The most enriched clone, Nb11, was progressively accumulated throughout the screening process (Fig. 3 *I* and *J*). Notably, Nb11 and Nb1B4 possess distinct CDR3 sequences (*SI Appendix*, Fig. S8*J*). The binding affinities of Nb11 was assessed via on-yeast titration assay (*SI Appendix*, Fig. S8*E*). Pharmacological assays demonstrate that Nb11 directly activates the M1R, albeit with low potency and efficacy compared to iperoxo, while moderately enhances the Emax of Ach (Fig. 3 *K* and *L* and *SI Appendix*, Fig. S8*I*).

Structure Insight of Nanobody–M1R Complexes. To better understand the molecular binding mode of the conformationally selective nanobodies, we attempted to resolve the complex structures of these nanobodies with the receptor. Unfortunately, the strong orientation preference of NbF3-bound and NbF7-bound complex samples prevented us from obtaining their three-dimensional structures. Finally, we successfully determined the cryo-EM structures of the active-state selective Nb1B4 bound to M1R-G_{11}CT complex with iperoxo, as well as the inactive-state selective NbA12 bound to M1R-Clip1 with atropine at global resolutions of 2.88 Å and 3.29 Å, respectively (Fig. 4 *A* and *B* and *SI Appendix*, Figs. S9 and S10). For Nb1B4, the structure reveals unambiguous electron density for Nb1B4–M1R interface. However, the datasets of NbA12-M1R still suffer from preferred orientation and the nanobody part exhibits discontinuous electron

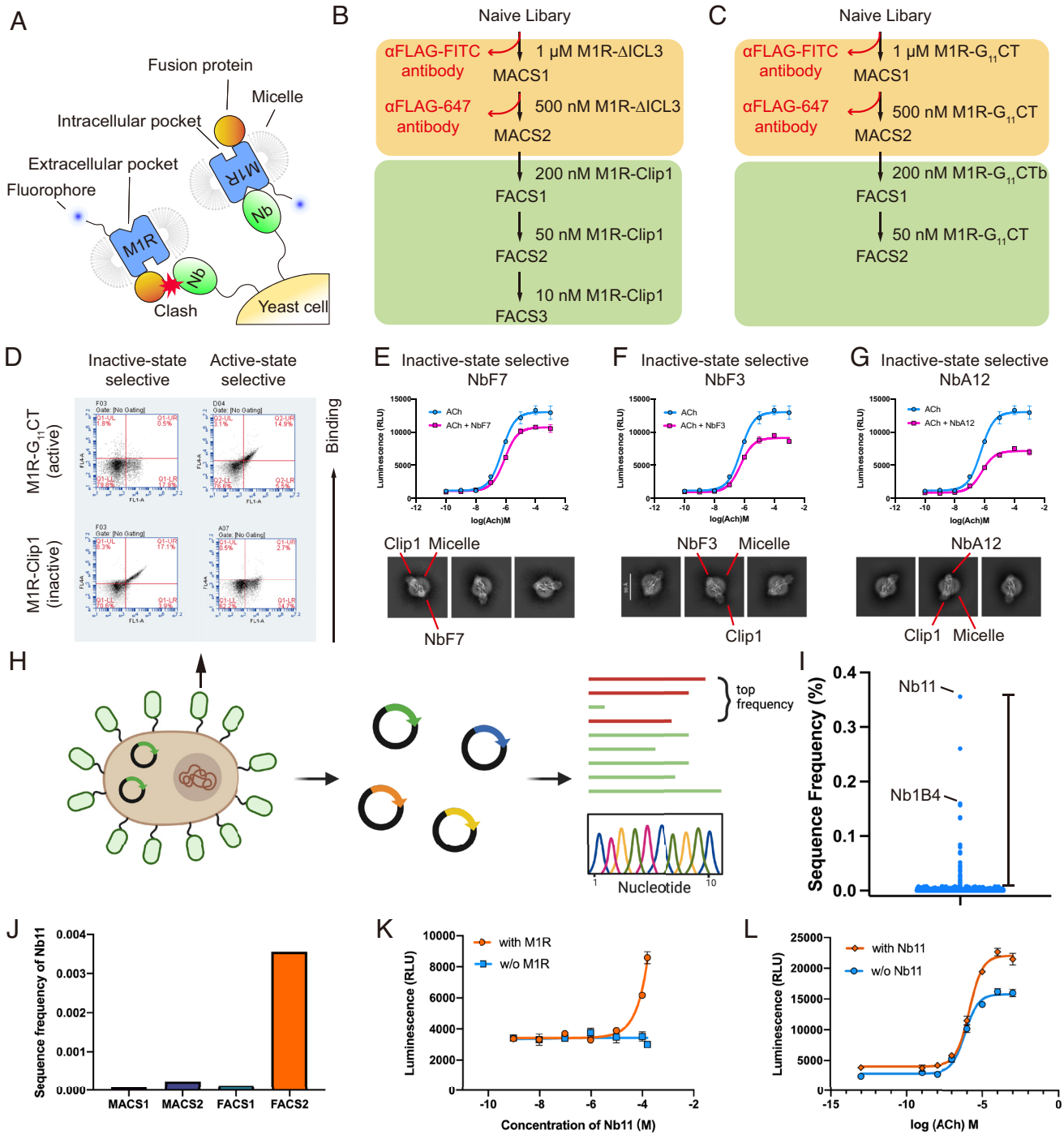

Fig. 3. Intracellular orthogonal screening for extracellular nanobodies. (*A*) Engineered proteins M1R-G_{11}CT, M1R-G_{11}CTb, and M1R-Clip1 demonstrate dual functionality: stabilizing distinct receptor conformations while preferentially enriching extracellular pocket-targeting nanobodies over intracellular-targeting counterparts during yeast display screening. (*B*) Schematic representation of the intracellular orthogonal screening approach for isolating inactive-state selective nanobodies. (*C*) Schematic representation of the intracellular orthogonal screening approach for isolating active-state selective nanobodies. (*D*) Yeast surface staining analysis, performed with 10 nM fluorescence-labeled receptors, validates the conformational selectivity of nanobodies, demonstrating their capacity to differentiate between receptor states. (*E–G*) Glo-sensor signaling assays reveal that inactive-state selective nanobodies (NbF7, NbF3, and NbA12) attenuate the maximal response (Emax) to endogenous agonist stimulation at 100 μM. (*H*) Schematic representation of the next-generation sequencing (NGS) workflow employed for active-state selective nanobody identification. (*I*) Nb11 and Nb1B4 demonstrate predominant enrichment profiles during active-state selective screening, emerging as the most abundant nanobody variants. (*J*) The progressive enrichment of Nb11 throughout the screening process. Functional characterization demonstrates that Nb11 exhibits partial agonist efficacy (*K*) and potentiates the maximal response of endogenous agonist signaling at 100 μM (*L*) in Glo-sensor assays. Data represent mean values ± SEM derived from three independent experimental replicates.

density, which prevented us from building a complete nanobody model. Despite this limitation, we were able to approximately localize the position of its CDR3 based on the available density (*SI Appendix*, Fig. S11*A*). The overall maps reveal that Nb1B4 and NbA12 share a similar scaffold binding pose, albeit with a rotational difference, when compared to MT7, a negative allosteric modulator (NAM) for M1R (11) (Fig. 4 *C* and *D*). This observation suggests that the extracellular vestibule of the muscarinic receptor is sufficiently spacious to accommodate diverse binding orientations, thereby facilitating the development

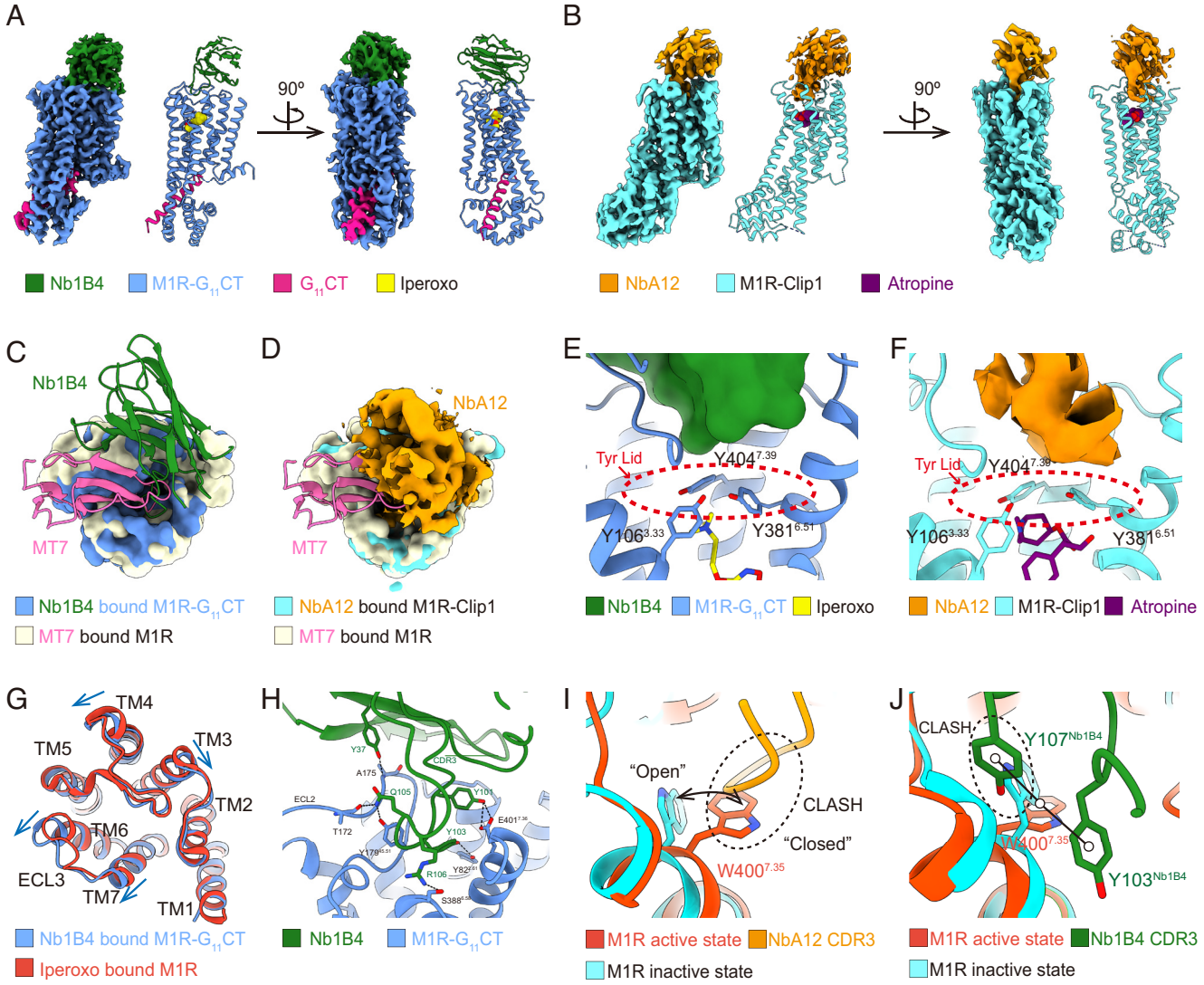

Fig. 4. Structure insight of nanobody–M1R complexes. (*A*) Overall cryo-EM density map and atomic model of the Nb1B4 and M1R-G_{11}CT complex bound to iperoxo. (*B*) Overall cryo-EM density map and refined atomic model of the NbA12 and M1R–Clip1 complex bound to atropine. The binding orientation of (*C*) Nb1B4 and (*D*) NbA12 are similar but distinct from that of MT7 (MT7 bound M1R, PDB: 6WJC). (*E*) Nb1B4 and (*F*) NbA12 bind to the allosteric pocket of M1R, positioned above the orthosteric pocket and tyrosine lid. (*G*) Nb1B4 binding induces outward displacement of TM6, TM7, and ECL3 compared to the iperoxo-bound M1R structure (PDB: 6OIJ). (*H*) Nb1B4 engages the extracellular vestibule of M1R through a broad network of polar interactions. (*I*) NbA12's CDR3 region exhibits conformational selectivity by accommodating the open state of $W400^{7.35}$ while sterically clashing with its closed state conformation. (*J*) Nb1B4's CDR3 region, particularly residues Y107 and Y103, demonstrates conformational selectivity by stabilizing the closed state of $W400^{7.35}$ while exhibiting steric clashes with its open state conformation.

of modulators targeting the receptor. Muscarinic receptors have long served as prototypic model systems for elucidating allosteric modulation of GPCR signaling. These structures confirmed that the CDR3 loops of Nb1B4 and NbA12 both occupy the conventional allosteric vestibule of M1R, located above the orthosteric site (Fig. 4 *E* and *F*). And the binding poses of the orthosteric ligands are similar to those observed in previously reported structures without nanobodies (*SI Appendix*, Fig. S11 *B* and *C*).

Nb1B4 is a distinctive nanobody identified to bind to the extracellular allosteric pocket of the active-state M1R with conformational selectivity (Fig. 3*D*). The high-resolution complex structure provides precise interaction details. Structure comparison between the M1R–Nb1B4–iperoxo complex and the nanobody-free M1R–iperoxo structure (PDB:6OIJ) reveals that Nb1B4 CDR3 insertion drives a slight outward movement of extracellular ends of TM6, TM7, and ECL3 (Fig. 4*G*). The Nb1B4 scaffold, along with its CDR3, engages in extensive polar interactions with the receptor's extracellular surface (Fig. 4*H*). The hydrogen bond network includes interactions between $Y37^{Nb1B4}$ with the backbone of the receptor's ECL2, and additional hydrogen bonds formed by $Y101^{Nb1B4}$ with $E401^{7.36}$, $Y103^{Nb1B4}$ with $Y82^{2.61}$, $Q105^{Nb1B4}$ with $Y179^{45.51}$, and the backbone of the receptor's ECL2 as well as $R106^{Nb1B4}$ with $S388^{6.58}$. These interactions were subsequently validated by site-directed mutagenesis (*SI Appendix*, Fig. S12). The Y37A, Q105A, and R106A mutations impaired nanobody–receptor binding. While the Y101A and Y103A single mutations had minimal impact, the Y101A/Y103A double mutation resulted in reduced binding affinity. Of note, this extracellular region of M1R has been identified in prior studies as a critical site for the function of allosteric modulators (11, 21, 40).

Conformational Selectivity Mechanism of Nanobodies. Structural comparisons have revealed several key factors influencing conformational selectivity. Overall, NbA12 binds to a broad pocket, similar to the allosteric pocket of the inactive-state M1R,

whereas Nb1B4 binds to a narrow pocket, resembling the allosteric pocket of the active-state M1R (*SI Appendix*, Fig. S11 *D* and *J*). Specifically, the CDR3 region of NbA12 is positioned closer to TM5, while that of Nb1B4 is located nearer to TM2 (*SI Appendix*, Fig. S11*E*). This spatial difference in CDR3 positioning underlies their distinct conformational preferences. The conformational changes in key amino acid residues modulate the morphology of the receptor's allosteric pocket between different states, with $W400^{7.35}$ playing a critical role. This residue directly links to the "Tyr lid" and undergoes a flip between the two states, a phenomenon highly conserved across the acetylcholine receptor family (*SI Appendix*, Fig. S11 *F* and *G*). In the active state, $W400^{7.35}$ adopts a "closed" conformation, while in the inactive state, it assumes an "open" conformation (Fig. 4*I*).

For NbA12, the closed conformation of $W400^{7.35}$ clashes with its backbone, restricting its binding to the active-state receptor (Fig. 4*I*). In contrast, for Nb1B4, the interaction interface is closer to TM2, providing sufficient space around $W400^{7.35}$ to accommodate its closed conformation. Additionally, $Y107^{Nb1B4}$ clashes with $W400^{7.35}$ in the open state, while $Y103^{Nb1B4}$ forms hydrophobic interactions with $W400^{7.35}$ in the closed state, stabilizing the latter conformation (Fig. 4*J* and *SI Appendix*, Fig. S11*H*). These structural and interactional nuances collectively enable Nb1B4 to selectively bind to the active-state receptor. Notably, the CDR3 of Nb1B4 forms a robust and conserved hydrogen bond network with TM7 and TM2, a feature also observed in the structures of positive allosteric modulators (PAMs) targeting M2R and M4R, such as LY2119620, LY2033298, and VU0467154 (*SI Appendix*, Fig. S11*I*) (21). This conserved interaction underscores the critical role of this site as a key allosteric binding hotspot within the muscarinic receptor family.

Discussion

GPCRs have long been recognized as crucial therapeutic targets, with both pharmaceutical industry and academic researchers dedicating decades of effort to novel ligand discovery. In recent years, binding-based drug discovery has emerged as a transformative approach in GPCR-targeted therapeutic development, demonstrating remarkable success through multiple breakthrough achievements. This approach has enabled significant milestones, including the application of DEL technology in identifying the first NAM and the first PAM for the β2AR, and the utilization of hybridoma screening in the development of Erenumab, which stands as the first FDA-approved GPCR-targeting antibody drug (41–44). The exceptional potential of binding-based drug discovery lies in its inherent advantages: the capability to target both orthosteric and allosteric binding pockets, the capacity to explore an extensive chemical space, and the facilitation of diverse ligand discovery encompassing antibodies, peptides, and small molecules.

It is widely recognized that obtaining a stable, purified receptor—exhibiting both thermal and structural stability—is a crucial prerequisite for successful binding-based screening. In this study, we investigated the feasibility of leveraging AI-driven approaches to design tool proteins that facilitate binding-based screening efforts. Building on our two previous studies, we refined the protein design method and successfully engineered M1R-Clip1, stabilized in the inactive state, and M1R-G_{11}CT, stabilized in the active state (33, 34). Notably, both the ligand-free tool proteins (M1R-Clip1 and M1R-G_{11}CT) exhibit significantly enhanced biochemical stability, a crucial feature for effective binding-based screening applications. Among these, M1R-G_{11}CT stands out with exceptional performance, demonstrating an approximately 600-fold improvement in agonist affinity. Remarkably, the agonist-independent active state of the engineered protein preserves the intact extracellular vestibule of the receptor, particularly the unoccupied orthosteric pocket for binding-based screening. Compared to our previous approach which relied on T4 lysozyme (T4L) fusion and disulfide bond stabilization (34), this workflow avoids the need of extensive construct screening. More significantly, it enables the efficient generation of a series of fusion proteins sharing the same scaffold but featuring distinct sequences, which we term intracellular orthogonal receptors. This advancement is pivotal for reducing screening noise attributable to the fusion protein itself, thereby enhancing the precision and reliability of the screening process.

Based on the designed proteins, we performed a proof-of-concept nanobody screening from a synthetic yeast surface display library. Antibodies targeting GPCRs have attracted considerable attention due to their exceptional selectivity and favorable pharmacokinetic properties. To overcome the challenges associated with conformationally selective antibody screening against the extracellular domains of GPCRs, several innovative approaches have been proposed. The core concept involves introducing or blocking diverse surfaces of the target protein to enrich nanobodies that specifically recognize particular epitopes (9, 45, 46). Our intracellular orthogonal screening strategy aligns with this rationale but offers significantly enhanced versatility and scalability. By utilizing tool proteins with distinct intracellular sequences but identical extracellular regions in each screening round, we successfully enriched nanobodies specifically targeting the extracellular domain. This approach ultimately enabled us to isolate a series of conformationally selective nanobodies against M1R.

The muscarinic receptor, a central therapeutic target for neuropsychiatric disorders like Alzheimer's and schizophrenia under the cholinergic hypothesis, has driven decades of research into selective agonists and PAMs. In this study, we introduce a series of extracellular nanobodies targeting M1R. Cryo-EM analysis reveals that these nanobodies bind to an allosteric pocket that undergoes conformational changes during receptor activation—a site shared by LY2119620 and muscarinic toxin MT7. Stabilizing this pocket to maintain the receptor conformation may represent a general mechanism for the allosteric modulation of muscarinic receptors. Moreover, these nanobodies are readily amenable to affinity maturation or biochemical optimization, enabling the enhancement of their binding affinity and functional activity in future research.

Materials and Methods

Computational Design of M1R-G_{11}CT and M1R-G_{11}CTb. M1R-G_{11}CT was engineered through an integrative computational design approach including RFdiffusion, ProteinMPNN, and AlphaFold2-Multimer (47–49), following the protocol previously employed for click fusion protein (Clip) design (33). The design process commenced with the extraction of the active-state M1R and α5 helix of G_{11} protein (residues 335-359, ENIRFVFAAVKDTILQLNLKEYNLV, G_{11}CT) complex from M1R-G_{11} protein complex (PDB: 6OIJ) as a substructure template. Subsequently, the ICL3 region of M1R was removed, and two residues at the membrane–cytosol interface of TM5/6 ($T215^{5.65}$ from TM5 and $A364^{6.34}$ from TM6) were selected as fusion site for backbone generation of the fusion protein while maintaining G_{11}CT as an independent input chain. G_{11}CT is important due to its critical role in guiding the proper folding of the fusion protein wrapping around it and stabilizing the active conformation of M1R. Reciprocally, the fusion protein rigidly linked to the receptor forms a suitable and stable binding pocket that constrains G_{11}CT in a specific orientation, creating a mutually stabilizing architecture. The backbone architecture of ~100-amino acid fusion protein was initially generated using RFdiffusion, followed by the side chain design through ProteinMPNN. Special attention was paid to ensuring that the designed fusion protein does not insert into the transmembrane region. Then, the structure of

the engineered active-state receptor was predicted using AlphaFold2-Multimer, with the receptor as one chain and G_{11}CT as another chain. The high pLDDT scores (pLDDT > 80) predicted by AlphaFold2-Multimer and low RMSD between the predicted structure and the target backbone are key criteria for evaluating the success of protein design. However, if the initial designs are not optimal, local refinement will be performed to generate improved variants. Specifically, we selected an AlphaFold-predicted structure with relatively high pLDDT scores as the starting model for optimization. During this process, we preserved regions with high pLDDT scores (pLDDT > 80) while performing local backbone regeneration or side-chain repacking in regions with low pLDDT scores. After iterative cycles of refinement, the amino acid sequence demonstrating high pLDDT scores (pLDDT > 80) was selected, and the corresponding DNA sequence encoding the fusion protein was synthesized for experimental characterization. For the M1R receptor, we selected a promising backbone with superior overall structural confidence (pLDDT > 80), and generated five rounds of local backbone refinement, producing 10 distinct backbone conformations per round along with four amino acid sequences for potential backbone (*SI Appendix*, Fig. S1). To enable intracellular orthogonal screening of extracellular nanobodies using engineered M1R variants, we strategically selected two constructs based on the following criteria: 1) maximal charge differences in fusion protein surface regions to ensure distinct intracellular epitope, while 2) maintaining superior structural confidence (pLDDT > 80), and 3) preserving characteristic active-state conformation. Finally, two DNA sequences encoding fusion proteins with identical backbone structures but distinct side chain configurations were synthesized (the annotated DNA sequences are provided in *SI Appendix*, Table S2). These protein constructs were designated as M1R-G_{11}CT and M1R-G_{11}CTb (the annotated receptor sequences are provided in *SI Appendix*, Table S1).

Computational Design of α_{1A}AR-G_{11}CT and μOR-G_iCT. For G_q/G_{11}-coupled α1A-adrenergic receptor (α_{1A}AR), the receptor and α5 helix (residues 222 to 246, ENARRIFNDCKDIILQMNLREYNLV, G_qCT) of the miniGαq_{iN} protein complex were extracted from α_{1A}AR-miniGαq_{iN} protein complex (PDB:8THK) as a substructure, followed by structural alignment to the M1R-G_{11}CT reference structure. Given the high structural similarity between α_{1A}AR and M1R, a chimeric construct was engineered by inserting the corresponding M1R-G_{11}CT fusion sequence between residues A211$^{5.65}$ (TM5) and K269$^{6.32}$ (TM6) of α_{1A}AR. The engineered α_{1A}AR-G_{11}CT structure was predicted using AlphaFold2-Multimer, with the receptor and α5 helix of G_{11} as separate chains. The resulting model exhibited high prediction confidence, particularly at the fusion interface. The α_{1A}AR-G_{11}CT construct with G_iCT linked to the C terminus of the receptor and fusion protein inserted to TM5/6 was generated for further in vitro validation (the annotated receptor sequence is provided in *SI Appendix*, Table S1).

For G_i/G_o-coupled μ-opioid receptor (μOR), the receptor and α5 helix of G_i protein (residues 327 to 354, TDTKNVQFVFDAVTDVIIKNNLKDCGLF, G_iCT) complex were extracted from the μOR-G_{i1} protein complex (PDB:8EFB) as a substructure, followed by structural alignment to the M1R-G_{11}CT reference structure. Similarly, the M1R-G_{11}CT fusion sequence was inserted into μOR between two sites (L261$^{5.65}$ from TM5 and R279$^{6.32}$ from TM6). However, structural divergence between the G_{11} and G_i α5-helices resulted in suboptimal performance of the direct transfer approach, as evidenced by low pLDDT scores. To address this, a refinement strategy was employed using the AlphaFold-predicted structure as the starting model, followed by side-chain repacking of the fusion protein. After one round of refinement, a protein model with proper folding characteristics was obtained, as demonstrated by significantly improved pLDDT scores (*SI Appendix*, Fig. S3). Finally, the codon-optimized DNA sequence encoding the optimized fusion protein between TM5 and TM6 was synthesized (the annotated DNA sequence is provided in *SI Appendix*, Table S2), generating the μOR construct with G_iCT linked to the C terminus of receptor, named μOR-G_iCT, for experimental validation (the annotated receptor sequence is provided in *SI Appendix*, Table S1).

Expression and Purification of the Receptors. The M1R constructs (M1R, M1R-ΔICL3, M1R-G_{11}CT, M1R-G_{11}CTb, and M1R-Clip1) were cloned into pFastBac vector for expression via the Bac-to-Bac Baculovirus system (Invitrogen). Sf9 cells were infected at a density of approximately 4.0×10^6 cells/mL and harvested 48 h postinfection. M1R-ΔICL3 expression was enhanced by supplementing 10 μM atropine during infection. Receptor purification was performed using Ni-NTA, Flag affinity chromatography, and SEC as described previously (6). Briefly, cell pellets were lysed in lysis buffer (10 mM HEPES, pH 7.5, 1 mM EDTA, 160 μg/mL benzamidine, 100 μg/mL leupeptin) for 30 min at room temperature. Following complete lysis, cell membranes were collected by centrifugation and solubilized using solubilization buffer (20 mM HEPES, pH 7.5, 750 mM NaCl, 1% dodecyl maltoside (DDM), 0.2% Na Cholate, 0.03% cholesterol hemisuccinate (CHS), 30% glycerol, 5 mM imidazole, 2 mM $MgCl_2$, 160 μg/mL benzamidine, 100 μg/mL leupeptin, 2 mg/mL iodoacetamide and benzonase), with continuous stirring at 4 °C for 2 h. After high-speed centrifugation, the supernatant was incubated with Ni-NTA resin for 2 h at 4 °C. The Ni-NTA resin, bound with receptor, was washed and then eluted with elution buffer (20 mM HEPES pH 7.5, 750 mM NaCl, 0.1% DDM, 0.02% Na Cholate, 0.03% CHS, 200 mM imidazole). Next, the elution from Ni-NTA resin was incubated with M1-Flag affinity resin with addition of 2 mM $CaCl_2$ and the detergent was gradually exchanged from DDM to 0.01% lauryl maltose neopentyl glycol (MNG). The receptor was eluted with 0.2 mg/mL Flag peptide and 5 mM EDTA, followed by further purification on a Sephadex 200 Increase 10/300 GL column (Cytiva) with a running buffer (20 mM HEPES pH 7.5, 0.01% MNG, 0.001% CHS, 100 mM NaCl). Finally, the purified receptor was concentrated using 50 kDa molecular weight cutoff Amicon centrifugal filters (Millipore).

Cryo-EM Grid Preparation. Purified M1R-G_{11}CT (4 μL) was deposited onto glow-discharged nickel-titanium grids (Ni-Ti R1.2/1.3, 300 mesh), while purified M1R–nanobody complexes (4 μL) were deposited onto glow-discharged Au Quantifoil grids (Au R1.2/1.3, 200 mesh). The grids were then gently blotted with Whatman No. 1 qualitative filter paper in a Vitrobot Mark IV (Thermo Fisher) chamber, which was maintained at 8 °C and 100% humidity. Blotting parameters were set to a blot time of 4 s and a blot force of four. Immediately after blotting, the grids were rapidly vitrified by plunging into liquid ethane.

Data Collection and Processing. Cryo-EM data of ligand-free M1R-G_{11}CT (1,960 micrographs), M1R-G_{11}CT–iperoxo–Nb1B4 complex (1,950 micrographs), M1R–Clip1–atropine–NbA12 complex (3,668 micrographs) were collected using Titan Krios G3i TEM (Thermo Fisher) equipped with an automated data collection (AutoEMation) (50). Data processing was conducted using a standardized workflow in cryoSPARC (v4.5.1) (51). Initial 2D classifications were carried out, and the highest-quality 2D averages were selected for 3D reconstruction. These averages were subsequently used as templates for particle picking across the entire dataset. Following multiple rounds of heterogeneous refinement and non-uniform refinement, a 3D volume with clear secondary structures was obtained. To focus on the transmembrane domain, detergent micelles in the 3D volume were masked out, enabling focused classification. After several iterations of heterogeneous refinement and 3D classification, high-resolution volumes were ultimately achieved. The final structure reconstructions utilized 155,176 particles for ligand-free M1R-G_{11}CT, 191,008 particles for the M1R-G_{11}CT–iperoxo–Nb1B4 complex, and 254,687 particles for the M1R–Clip1–atropine–NbA12 complex, yielding resolutions of 3.62 Å, 2.88 Å, and 3.29 Å, respectively.

Model Building and Refinement. The initial structural models of M1R-G_{11}CT, M1R-Clip1, Nb1B4, and NbA12 were generated from AlphaFold2 predictions. Coordinates and chemical constraints for atropine and iperoxo were created using Phenix.elbow (1.20.1 to 4,487) (52). These models were then fitted into the Cryo-EM density maps using UCSF ChimeraX-1.3 (53), followed by manual adjustments and refinements in COOT-0.9.8.7 (54). Final structural refinement and validation were carried out using PHENIX (55).

Cell Surface Staining. Cell surface staining was performed to assess receptor expression levels. Briefly, transfected cells were resuspended in phosphate buffer solution (PBS) containing 2 mM $CaCl_2$ and incubated with Alexa-488 conjugated anti-Flag antibody (diluted in HBSS at a ratio of 1:300, Thermo Fisher, Cat # MA1-142-A488) for 15 min at room temperature in the dark. Then the cells were washed twice with PBS containing 2 mM $CaCl_2$. Nonspecific binding was evaluated using negative control samples containing 0.2 mg/mL Flag peptide. Fluorescence measurements were then performed using a BD Accuri C6 flow cytometer (BD Biosciences), with excitation at 488 nm and emission at 519 nm. Cells were gated by cell size and granularity to ensure accurate analysis.

Radioligand Binding Assays. The M1R constructs, including M1R-G_{11}CT, M1R-Clip1, M1R-ΔICL3, and M1R-miniGsq, α_{1A}AR-G_{11}CT, α_{1A}AR-wt, μOR-G_iCT, and μOR-wt were expressed in either Sf9 insect cells or HEK293F mammalian cells.

Membrane fractions were prepared by harvesting 50 mL of cell culture, followed by homogenization in 8 mL of ice-cold lysis buffer (20 mM Tris, pH 7.5, 1 mM EDTA). The homogenate was subjected to sequential centrifugation: first at 800 rpm for 10 min to remove cellular debris, then the supernatant was centrifuged at 18,000 rpm for 20 min to pellet membranes. The final membrane fraction was resuspended in binding buffer (20 mM HEPES, pH 7.5, 100 mM NaCl). For saturation binding assays, membranes were incubated with varying concentrations of hot ligand ([^{3}H]-NMS for M1R, [^{3}H]-prazosin for α_{1A}AR and [^{3}H]-DPN for μOR) in binding buffer (20 mM HEPES, pH 7.5, 100 mM NaCl, 5 mM $MgCl_2$, and 0.1% BSA) for 1 h at room temperature. Antagonist (10 μM atropine for M1R, 10 μM prazosin for α_{1A}AR, 10 μM naloxone for μOR) was used to define nonspecific binding. For competition binding experiments, membranes were incubated with a constant concentration of hot ligand alongside increasing concentrations of corresponding agonist or antagonist for 60 min at room temperature to determine ligand binding affinities for receptor variants. Binding reactions were rapidly filtered through GF/B filters using Brandel 48-well harvester. Filters were washed three times with ice-cold binding buffer and immersed in scintillation fluid. Bound radioactivity was quantified using a liquid scintillation counter (MicroBeta2, PerkinElmer), and the data were analyzed with Prism 9 (GraphPad).

Conformationally Selective Nanobody Screening. The synthetic nanobody library displayed on the yeast surface was generously provided by Drs. A. C. Kruse (Harvard University) and A. Manglik (University of California San Francisco) (9). Yeast cells were cultured in tryptophan dropout (-Trp) medium supplemented with 2% (w/w) glucose at 30 °C. Nanobody expression was induced by transferring the cells to -Trp medium containing 2% (w/w) galactose, followed by culturing for 2 d at 25 °C. Nanobody expression levels were assessed by staining with Alexa Fluor-488–conjugated anti-HA antibody (Cell Signaling Technology) and analyzed via flow cytometry using an Accuri C6 (BD Biosciences).

Nanobody clones targeting the different purified FLAG-tagged M1R constructs were enriched through two rounds of MACS and two or three rounds of FACS using FACSAria II (BD Biosciences) in selection buffer (20 mM HEPES pH 7.5, 100 mM NaCl, 0.05% MNG, 0.005% CHS, 2 mM $CaCl_2$, 0.1% (w/v) bovine serum albumin and 0.2% maltose), as previously reported (Fig. 3 *B* and *C*) (56). For the first and second rounds of MACS, 5×10^9 and 2×10^8 induced yeast cells were used as input, respectively. The yeast cells were washed and precleared by incubating with Alexa Fluor–FITC–conjugated anti–FLAG antibody and anti–Alexa Fluor–FITC microbeads (Miltenyi) (or Alexa Fluor–647–conjugated anti-FLAG antibody and anti-Alexa Fluor-647 microbeads), followed by passage through an LD column (Miltenyi) to remove yeast displaying nonspecific nanobodies. The flow-through yeast cells were washed with selection buffer, and then incubated with FLAG-tagged M1R construct bound to ligand (atropine for inactive-state selective nanobody screening, iperoxo for active-state selective nanobody screening), Alexa Fluor-FITC-conjugated anti-FLAG antibody and anti-Alexa Fluor–FITC microbeads (or Alexa Fluor–647–conjugated anti-FLAG antibody and anti-Alexa Fluor–647 microbeads). After incubation at 4 °C for 30 min, the yeast cells were loaded onto an LS column, washed with selection buffer and eluted by plunger.

Subsequently, several rounds of FACS were performed using FACSAria II (BD Biosciences) (*SI Appendix*, Fig. S7). For each round, 2×10^7 yeast cells were stained with Alexa Fluor–488–conjugated anti-HA antibody (Cell Signaling Tech), Alexa Fluor–647–conjugated anti–FLAG antibody and FLAG-tagged M1R construct bound with ligand (atropine for inactive-state selective nanobody screening, iperoxo for active-state selective nanobody screening) in the selection buffer. After screening, the sorted yeast cells were diluted and plated on -Trp agar plates, and single colonies were picked and cultured as clonal populations in deep 96-well plates for nanobody binder screening. For yeast surface staining, the nanobody displayed yeast cells were stained with the Alexa Fluor–488–conjugated anti-HA antibody (Cell Signaling Tech), purified FLAG-tagged M1R and Alexa Fluor–647–conjugated anti-FLAG antibody in the selection buffer, and analyzed by Accuri C6 (BD Biosciences). The double-positive staining yeast cells among the anti-HA positive population were selected for sequencing analysis.

On-Yeast Titration Assay. On-yeast titration assay was performed according to previously published protocols with minor modifications (11). Nb11 was cloned to pYDS649 plasmid and transformed into TBY100 (9). Briefly, expression induced yeast cells were washed twice with cold selection buffer and incubated with FLAG-tagged M1R preincubated with 10 μM atropine or 10 μM iperoxo at each concentration for 30 min on ice. Following incubation, the cells were washed twice with cold selection buffer to remove unbound receptors. Subsequently, the yeast cells were incubated with Alexa Fluor–647–conjugated anti–FLAG antibody for 15 min on ice and then washed twice with cold selection buffer. Finally, the cells were resuspended in cold selection buffer with Alexa Fluor–488–conjugated anti-HA antibody and the fluorescence signals were acquired using Accuri C6 (BD Biosciences). The receptor-bound fraction was determined by calculating the ratio of double-positive cells and was normalized by setting the highest observed binding fraction within each experiment to 100%.

Expression and Purification of Nanobodies. Selected yeast clones were sequenced and the corresponding nanobody sequences were subcloned into the pET26b periplasmic expression vector featuring an N-terminal pelB signal peptode and a C-terminal histidine tag, and then transformed into BL21(DE3) *Escherichia coli*. Cells were grown in Terrific Broth (TB) medium supplemented with 2 mM $MgCl_2$, 0.1% glucose, and 50 μg/mL kanamycin at 37 °C until reaching an OD_{600} of 1.0. Protein production was induced with 1 mM IPTG, and the culture was incubated at 20 °C for 20 h with shaking. Periplasmic extraction was performed via osmotic shock, cells were resuspended in cold hypertonic buffer (0.2 M Tris-HCl, pH 8.0, 0.5 mM EDTA, 0.5 M sucrose) for 1 h at 4 °C, then diluted fourfold with ice-cold water for additional hypotonic treatment. After high-speed centrifugation, the supernatant was purified using Ni-NTA resin followed by SEC with running buffer (20 mM HEPES, pH7.5, 100 mM NaCl). In addition to the *E. coli* expression system, some nanobodies such as NbF3, NbF7, NbA12, and Nb1B4 were expressed in the HEK293F transient expression system. These nanobodies were subcloned into pcDNA3.4 vector with an N-terminal Mouse Ig Heavy chain signal peptide and a C-terminal histidine tag, cells were transfected with Polyethylenimine (PEI) at a density of 2.0×10^6 cells/mL and cultured at 37 °C for 3 to 4 d. The culture supernatants were harvested for nanobody purification using Ni-NTA resin and SEC. Finally, the purified nanobodies were concentrated to 10 to 40 mg/mL using 10 kDa molecular weight cutoff Amicon centrifugal filters (Millipore).

Next-Generation Sequencing. To track sequence evolution throughout the selection process, nanobody-encoding regions were PCR-amplified from yeast plasmid populations using primers (seq-F: 5′-CCTGCGCCTGAGCTGCG-3′, seq-R: 5′-GCTGCTCACGGTCACCTGGG-3′). The PCR products were sent to Sangon Biotech (Shanghai, China) Co.Ltd for sequencing library preparation and subsequent paired-end sequencing (PE300) on the Illumina platform, with raw reads processed through NGmerge for pair merging. Quality-filtered sequences were translated and analyzed for amino acid frequency distributions using custom scripts.

Glo-Sensor Signaling Assay. A Gsq chimera, constructed by replacing the last 15 amino acids of C terminus of Gs protein with the last 15 amino acids of Gq protein, was used to measure Gq signaling using Glo-sensor assay (57). To perform the assay, HEK293T cells were seeded in a six-well plate and allowed to grow to 50 to 80% confluence prior to transfection. A plasmid mixture containing 250 ng M1R-wt, 250 ng Gsq, and 3,750 ng pGloSensor™-22F plasmid (Promega) in 250 μL of Opti-MEM (Gibco) was transfected into cells using 12.5 μL 1 mg/mL PEI. 24 h posttransfection, cells were harvested from the plate and resuspended in 5 mL Hanks' Balanced Salt Solution (HBSS) supplemented with 20 mM HEPES, pH 7.5, and 150 μg/mL luciferin, and then transferred to a 96-well plate at 70 μL per well. After incubation at 37 °C for 1 h followed by an additional hour at room temperature, 20 μL of different concentrations of nanobodies and 10 μL of acetylcholine (Ach) were added, and luminescence counts were measured by Ensight™ plate reader (PerkinElmer). For the inactive-state selective nanobodies, a 20-min preincubation with nanobodies was performed before Ach addition. Data analysis was conducted using Prism 9 (GraphPad).

NanoBiT Based β-Arrestin Recruitment Assay. NanoBiT based β-arrestin recruitment assays were performed following a previously published protocol with minor modifications (58). Briefly, Hek293T cells were transfected with corresponding plasmids using PEI as transfection reagent at a DNA:PEI ratio of 1:3. 1.3 μg of receptor-SmBiT (with M2R-M5R constructs containing the V2Rpp sequence at the C terminus, except for the M1R-wt construct) and 1.3 μg of LgBiT-β-arrestin1 were used. After 18 to 20 h of transfection, cells were harvested in DMEM, centrifuged, and resuspended in 5 mL HBSS buffer supplemented with 10 mM HEPES, pH7.5, and coelenterazine. The cells were then seeded in a white, flat-bottom, 96-well plate at 70 μL per well. The plate was incubated at room temperature for 60 min to allow for equilibration. Nanobodies were added at the final concentration of 100 μM and

incubated for 20 min, followed by recording the luminescence counts as the basal reading using Ensight™ plate reader (PerkinElmer). The cells were subsequently simulated with varying doses of Ach (10 μL per well) prepared in buffer (20 mM HEPES, pH7.5, 100 mM NaCl), and luminescence was recorded. Data analysis was conducted using Prism 9 (GraphPad).

Data, Materials, and Software Availability. Structure map and model data have been deposited in Protein Data Bank (9UCP (59), 9UAP (60), and 9UAZ (61)).

ACKNOWLEDGMENTS. This work was supported by Beijing Frontier Research Center for Biological Structure, and Tsinghua-Peking Center for Life Sciences, Tsinghua University (X.L.), by National Natural Science Foundation of China (Grant 32122041 to X.L.) and by Tsinghua University Initiative Scientific Research Program (X.L.). We gratefully acknowledge Drs. A. C. Kruse (Harvard University) and A. Manglik (University of California San Francisco) for supplying the synthetic nanobody library, and Dr. A. Inoue (Kyoto University) for providing the plasmids for the NanoBiT assay. We thank the Tsinghua University Branch of China National Center for Protein Sciences (Beijing) for support with cryo-EM data collection, and the Radioisotope Laboratory and Flow Cytometry Sorting Facility, Center of Biomedical Analysis, Tsinghua University, for technical support in radioligand binding experiments and flow cytometry sorting.

1. A. S. Hauser *et al.*, Trends in GPCR drug discovery: New agents, targets and indications. *Nat. Rev. Drug Discov.* **16**, 829–42 (2017).
2. L. Cheng *et al.*, Structure, function and drug discovery of GPCR signaling. *Mol. Biomed.* **4**, 46 (2023).
3. P. Conflitti *et al.*, Functional dynamics of G protein-coupled receptors reveal new routes for drug discovery. *Nat. Rev. Drug Discov.* **24**, 251–275 (2025).
4. D. Hilger, M. Masureel, B. K. Kobilka, Structure and dynamics of GPCR signaling complexes. *Nat. Struct. Mol. Biol.* **25**, 4–12 (2018).
5. W. I. Weis, B. K. Kobilka, The molecular basis of G protein-coupled receptor activation. *Annu. Rev. Biochem.* **87**, 897–919 (2018).
6. S. Maeda *et al.*, Structures of the M1 and M2 muscarinic acetylcholine receptor/G-protein complexes. *Science* **364**, 552–557 (2019).
7. S. G. F. Rasmussen *et al.*, Structure of a nanobody-stabilized active state of the β2 adrenoceptor. *Nature* **469**, 175–80 (2011).
8. D. Yang *et al.*, G protein-coupled receptors: Structure- and function-based drug discovery. *Signal Transduction Targeted Ther.* **6**, 7 (2021).
9. C. McMahon *et al.*, Yeast surface display platform for rapid discovery of conformationally selective nanobodies. *Nat. Struct. Mol. Biol.* **25**, 289–296 (2018).
10. A. A. Peterson, D. R. Liu, Small-molecule discovery through DNA-encoded libraries. *Nat. Rev. Drug Discov.* **22**, 699–722 (2023).
11. S. Maeda *et al.*, Structure and selectivity engineering of the M(1) muscarinic receptor toxin complex. *Science* **369**, 161–167 (2020).
12. J. Zhao *et al.*, Ligand efficacy modulates conformational dynamics of the μ-opioid receptor. *Nature* **629**, 474–480 (2024).
13. J. Xu *et al.*, Structural and dynamic insights into supra-physiological activation and allosteric modulation of a muscarinic acetylcholine receptor. *Nat. Commun.* **14**, 376 (2023).
14. A. Manglik, B. K. Kobilka, J. Steyaert, Nanobodies to study G protein-coupled receptor structure and function. *Annu. Rev. Pharmacol. Toxicol.* **57**, 19–37 (2017).
15. X. Ma *et al.*, Analysis of beta(2)AR-G(s) and beta(2)AR-G(i) complex formation by NMR spectroscopy. *Proc. Natl. Acad. Sci. U.S.A.* **117**, 23096–23105 (2020).
16. A. Manglik *et al.*, Structural insights into the dynamic process of beta2-adrenergic receptor signaling. *Cell* **161**, 1101–1111 (2015).
17. J. Heng *et al.*, Function and dynamics of the intrinsically disordered carboxyl terminus of β2 adrenergic receptor. *Nat. Commun.* **14**, 2005 (2023).
18. G. G. Gregorio *et al.*, Single-molecule analysis of ligand efficacy in β2AR–G-protein activation. *Nature* **547**, 68–73 (2017).
19. T. Fontaine *et al.*, Structure elucidation of a human melanocortin-4 receptor specific orthosteric nanobody agonist. *Nat. Commun.* **15**, 7029 (2024).
20. E. S. O'Brien *et al.*, A μ-opioid receptor modulator that works cooperatively with naloxone. *Nature* **631**, 686–693 (2024).
21. A. C. Kruse *et al.*, Activation and allosteric modulation of a muscarinic acetylcholine receptor. *Nature* **504**, 101–106 (2013).
22. M. M. Papasergi-Scott *et al.*, Time-resolved cryo-EM of G-protein activation by a GPCR. *Nature* **629**, 1182–1191 (2024).
23. A. J. H. Brown *et al.*, From structure to clinic: Design of a muscarinic M1 receptor agonist with potential to treatment of Alzheimer's disease. *Cell* **184**, 5886–901.e22 (2021).
24. P. Jeffrey Conn, A. Christopoulos, C. W. Lindsley, Allosteric modulators of GPCRs: A novel approach for the treatment of CNS disorders. *Nat. Rev. Drug Discov.* **8**, 41–54 (2009).
25. C. C. Felder *et al.*, Current status of muscarinic M1 and M4 receptors as drug targets for neurodegenerative diseases. *Neuropharmacology* **136**, 449–458 (2018).
26. A. B. Tobin, A golden age of muscarinic acetylcholine receptor modulation in neurological diseases. *Nat. Rev. Drug Discov.* **23**, 743–758 (2024).
27. I. Kaul *et al.*, Efficacy and safety of the muscarinic receptor agonist KarXT (xanomeline-trospium) in schizophrenia (EMERGENT-2) in the USA: Results from a randomised, double-blind, placebo-controlled, flexible-dose phase 3 trial. *Lancet* **403**, 160–170 (2024).
28. J. S. Lorente *et al.*, GPCR drug discovery: New agents, targets and indications. *Nat. Rev. Drug Discov.* **24**, 458–479 (2025).
29. T. W. M. de Groof *et al.*, Nanobodies: New avenues for imaging, stabilizing and modulating GPCRs. *Mol. Cell. Endocrinol.* **484**, 15–24 (2019).
30. R. R. Schlimgen *et al.*, Structural basis for selectivity and antagonism in extracellular GPCR-nanobodies. *Nat. Commun.* **15**, 4611 (2024).
31. M. A. Skiba *et al.*, Antibodies expand the scope of angiotensin receptor pharmacology. *Nat. Chem. Biol.* **20**, 1577–1585 (2024).
32. R. W. Cheloha *et al.*, Improved GPCR ligands from nanobody tethering. *Nat. Commun.* **11**, 2087 (2020).
33. K. Gao *et al.*, De novo design of a fusion protein tool for GPCR research. *Proc. Natl. Acad. Sci. U.S.A.* **122**, e2422360122 (2025).
34. X. Liu *et al.*, Structural insights into the process of GPCR-G protein complex formation. *Cell* **177**, 1243–51.e12 (2019).
35. P. Scheerer *et al.*, Crystal structure of opsin in its G-protein-interacting conformation. *Nature* **455**, 497–502 (2008).
36. B. Carpenter *et al.*, Structure of the adenosine A2A receptor bound to an engineered G protein. *Nature* **536**, 104–107 (2016).
37. H. Götzke *et al.*, The ALFA-tag is a highly versatile tool for nanobody-based bioscience applications. *Nat. Commun.* **10**, 4403 (2019).
38. A. M. Ring *et al.*, Adrenaline-activated structure of β2-adrenoceptor stabilized by an engineered nanobody. *Nature* **502**, 575–579 (2013).
39. J. R. Lane *et al.*, Protean agonism at the dopamine D2 receptor: (S)-3-(3-hydroxyphenyl)-N-propylpiperidine is an agonist for activation of Go1 but an antagonist/inverse agonist for Gi1, Gi2, and Gi3. *Mol. Pharmacol.* **71**, 1349–1359 (2007).
40. J. Wang *et al.*, The unconventional activation of the muscarinic acetylcholine receptor M4R by diverse ligands. *Nat. Commun.* **13**, 2855 (2022).
41. C. T. King *et al.*, Discovery of the migraine prevention therapeutic Aimovig (erenumab), the first FDA-approved antibody against a G-protein-coupled receptor. *ACS Pharmacol. Transl. Sci.* **2**, 485–490 (2019).
42. X. Liu *et al.*, Mechanism of intracellular allosteric β2AR antagonist revealed by X-ray crystal structure. *Nature* **548**, 480–484 (2017).
43. S. Ahn *et al.*, Allosteric "beta-blocker" isolated from a DNA-encoded small molecule library. *Proc. Natl. Acad. Sci. U.S.A.* **114**, 1708–1713 (2017).
44. X. Liu *et al.*, Mechanism of beta(2)AR regulation by an intracellular positive allosteric modulator. *Science* **364**, 1283–1287 (2019).
45. M. A. Skiba *et al.*, Epitope-directed selection of GPCR nanobody ligands with evolvable function. *Proc. Natl. Acad. Sci. U.S.A.* **122**, e2423931122 (2025).
46. C. McMahon *et al.*, Synthetic nanobodies as angiotensin receptor blockers. *Proc. Natl. Acad. Sci. U.S.A.* **117**, 20284–20291 (2020).
47. J. L. Watson *et al.*, De novo design of protein structure and function with RFdiffusion. *Nature* **620**, 1089–1100 (2023).
48. J. Jumper *et al.*, Highly accurate protein structure prediction with AlphaFold. *Nature* **596**, 583–589 (2021).
49. J. Dauparas *et al.*, Robust deep learning–based protein sequence design using ProteinMPNN. *Science* **378**, 49–56 (2022).
50. J. Lei, J. Frank, Automated acquisition of cryo-electron micrographs for single particle reconstruction on an FEI Tecnai electron microscope. *J. Struct. Biol.* **150**, 69–80 (2005).
51. A. Punjani *et al.*, CryoSPARC: Algorithms for rapid unsupervised cryo-EM structure determination. *Nat. Methods* **14**, 290–296 (2017).
52. N. W. Moriarty, R. W. Grosse-Kunstleve, P. D. Adams, electronic Ligand Builder and Optimization Workbench (eLBOW): A tool for ligand coordinate and restraint generation. *Acta Crystallogr. D, Biol. Crystallogr.* **65**, 1074–1080 (2009).
53. E. C. Meng *et al.*, UCSF chimeraX: Tools for structure building and analysis. *Protein Sci.* **32**, e4792 (2023).
54. P. Emsley, K. Cowtan, Coot: Model-building tools for molecular graphics. *Acta Crystallogr. D, Biol. Crystallogr.* **60**, 2126–2132 (2004).
55. D. Liebschner *et al.*, Macromolecular structure determination using X-rays, neutrons and electrons: Recent developments in Phenix. *Acta Crystallogr. D, Struct. Biol.* **75**, 861–877 (2019).
56. Y. Toyoda *et al.*, Structural basis of α1A-adrenergic receptor activation and recognition by an extracellular nanobody. *Nat. Commun.* **14**, 3655 (2023).
57. X. Lv *et al.*, Structures of human prostaglandin F2α receptor reveal the mechanism of ligand and G protein selectivity. *Nat. Commun.* **14**, 8136 (2023).
58. A. B. Kleist *et al.*, Conformational selection guides beta-arrestin recruitment at a biased G protein-coupled receptor. *Science* **377**, 222–228 (2022).
59. X. Zhang, K. Gao, X. Liu, cryo-EM structure of M1 muscarinic acetylcholine receptor-alpha5 helix of G11 protein complex bound to iperoxo and nanobody Nb1B4. Protein Data Bank. https://www.rcsb.org/structure/9UCP. Deposited 7 April 2025.
60. X. Zhang, K. Gao, X. Liu, cryo-EM structure of ligand-free active-state M1 muscarinic acetylcholine receptor with alpha5 helix of G11 protein complex. Protein Data Bank. https://www.rcsb.org/structure/9UAP. Deposited 3 April 2025.
61. X. Zhang, K. Gao, X. Liu, cryo-EM structure of the M1 muscarinic acetylcholine receptor bound to atropine and nanobody NbA12. Protein Data Bank. https://www.rcsb.org/structure/9UAZ. Deposited 3 April 2025.